# Combat molten aluminum corrosion of AISI H13 steel by lowtemperature liquid nitrocarburizing

Chen, Guang; Wang, Jun ; Fan, Hongyuan; Wang, Danqi; Li, Xiaoying; Dong, Hanshan

*DOI:*
10.1016/j.jallcom.2018.10.298



*Document Version*
Peer reviewed version

*Citation for published version (Harvard):*
Chen, G, Wang, J, Fan, H, Wang, D, Li, X & Dong, H 2019, 'Combat molten aluminum corrosion of AISI H13 steel by lowtemperature liquid nitrocarburizing', *Journal of Alloys and Compounds*, vol. 776, pp. 702-711. https://doi.org/10.1016/j.jallcom.2018.10.298

# Combat molten aluminum corrosion of AISI H13 steel by low-temperature liquid nitrocarburizing

Guang Chen[1], Jun Wang[1*], Hongyuan Fan[1], Danqi Wang[2], Xiaoying Li[3], Hanshan Dong[3]

*1. School of manufacturing science and engineering, Sichuan University, Chengdu, Sichuan (610065), China*

*2. Swagelok Center for Surface Analysis of Materials, Case Western Reserve University, 10900 Euclid Ave, Cleveland, 44106, US*

*3. School of Metallurgy and Materials, the University of Birmingham, Birmingham B15 2TT, UK*

## Highlights

- Molten aluminum corrosion resistance of AISI H13 steel was significantly improved.
- Duplex oxide layer significantly improved molten aluminum corrosion resistance.
- Phase transformations for H13 steel during liquid nitrocarburizing was determined.
- Activation energy for liquid nitrocarburizing is 195.4 kJ $mol^{-1}$.

## Abstract

Possibility of improving the resistance of AISI H13 steel to molten aluminum corrosion by liquid nitrocarburizing (LNC) was explored. The effects of the LNC parameters in terms of temperatures (703/723/743K) and soaking time (4/8/12h) on phase transformation, microstructure, and resistance to molten aluminum were fully studied. The surface phase compositions and the cross-sectional phase distribution of the LNC treated specimens were studied by implementable X-ray diffraction analysis. Microstructure, element distribution, microhardness, and the kinetics of the nitrocarburized case formation were fully researched. Immersion test of corrosion resistance to molten aluminum was carried out at 1023K for 30min. It is observed that an oxide layer can be produced on the top of the nitrocarburized case during LNC treatment, which cannot be regularly produced by other nitriding methods. The nitrocarburized case consists of a compound layer, a diffusion layer, and a transition layer. The growth of the nitrocarburized case is proportional to the squared treatment time and follows the Arrhenius law for the treatment temperature. The activation energy is estimated to be 195.4 kJ·$mol^{-1}$. While the nitrocarburized case provided

* Corresponding Author: School of Manufacturing Science and Engineering, Sichuan University, Chengdu, Sichuan 610065, China
E-mail address: srwangjun@scu.edu.cn (J.Wang)

limited resistance to molten aluminum, the oxide layer formed on the top of the nitrocarburized case conferred significantly improved molten aluminum corrosion resistance, especially a duplex oxide layer produced at 743K.

## Key Words

AISI H13 steel; Low-temperature liquid nitrocarburizing; Molten aluminum corrosion resistance; Microstructure; Kinetics

## 1. Introduction

AISI H13 steel is widely used in hot working processes where environments are very harsh. These processes can be characterized by high working temperatures (> 873K) and high abrasion. AISI H13 steel is commonly used as moulding and casting die materials due to its high strength and decent ductility, good tempering resistance, and moderate cost [1, 2]. Hot extrusion, casting and injection are regularly work processes for aluminum products such as beams, tubes, rods, et al [3]. Die steel surfaces are frequently in contact with high-temperature molten aluminum.

Aluminum is one of the most corrosive liquid metals due to its high chemical activity, which enables it to react with nearly all metals and metal oxides [4-6]. Therefore, corrosion and erosion caused by molten aluminum significantly reduce the service life of tool for liquid aluminum processing (such as die casting, hot-dip aluminizing, etc.) [7-9]. One cost-effective method is surface treatments to protect the tool materials against the attack of the molten aluminum [6].

Nitriding is a thermochemical process widely used for iron-based alloys. Diffusion of nitrogen into the materials surface can significantly enhance the wear and corrosion resistance of the alloy. Usually, nitriding is applied as a surface treatment to produce a compound layer composed of iron nitrides ( $\varepsilon$ and/or $\gamma'$) on the surface of the work pieces [10]. The microstructures and properties of the compound layer are directly correlated with the occurrence of the phase transformations, which are governed by the nitrocarburizing parameters, such as nitriding temperature and time [11]. Previously, the following phase transformation mechanism for the layer has generally been accepted: $\alpha$-Fe + N/C$\rightarrow$ $\varepsilon$ $\rightarrow$ $\gamma'$ [12]. More recently, literatures [13, 14] have offered contradictory findings about the phase transformation mechanism of austenite steel: $\gamma$-Fe + N/C $\rightarrow$ $\gamma_N$ + N/C $\rightarrow$ $\gamma'$ + N/C $\rightarrow$ $\varepsilon$. A new nitride with martensite structure ($\alpha'$-Fe) was proposed and referred as nitrogen-containing tetragonal martensite $\alpha'_N$-Fe [15-18]. However, very few researchers paid attention to the phase transformation mechanism of the martensite in liquid nitrocarburizing process.

Literatures [19, 20] demonstrated that the wear resistance of steel can be significantly

improved by nitriding treatment. However, according the investigation of Doche et al. [21], gas nitriding treatments alone do not significantly improve the general corrosion resistance of steels, and may even promote localized corrosion when the specimens were immersed for long time in saline solutions. Moreover, Karimzadeh et al. and Abedi et al. [22, 23] showed that the corrosion resistance of steels was compromised by nitriding, while post-oxidizing treatment could improve the uniform and localized corrosion resistance as well as wear resistance. Besides, all oxidation treatments of AISI H13 tool steel promote formation of a passive oxide film, which contributed to improved corrosion and erosion resistance to molten aluminum [24-26]. Hence, in order to improve the corrosion resistance, the post-oxidizing treatment is essential for gas nitriding treatment.

Liquid nitrocarburizing is a traditional and cost-effective method and has its unique advantages such as broad spectrum of tool shape that can be treated, simplicity of operation, low part distortion, environmental-friendly, and reproducibility [27, 28]. In addition, an oxide layer on top of the nitrocarburized case can be simultaneously produced by liquid nitrocarburizing process without additional post-oxidizing treatment. However, liquid nirocarbutizing of AISI H13 steel and whether this treatment can improve the corrosion resistance to molten aluminum were rarely researched. Recent works has shown that low-temperature nitriding contributes to enhanced pitting resistance [29] and low processing temperature minimizes part dimension distortion [30]. Therefore, low-temperatures (703/723K/743K) liquid nitrocarburizing has applied to AISI H13 die steel in this study.

The goal of the present work is to present original results on the AISI H13 steel surface hardening by low-temperature liquid nitrocarburizing, aiming to improve the corrosion resistance of H13 to molten aluminum. In addition, the effects of treatment temperature and time on the phase transformation, microstructure and treated layer growth kinetics have also been investigated.

# 2. Experiments

## 2.1 Materials and LNC treatments

AISI H13 steel was used in this study with a chemical composition (wt.%) of: 0.38 C, 0.1 Si, 0.4 Mn, 5 Cr, 1.4 Mo, 1 V, ≤0.030 P, ≤0.030 S, and balance Fe. Specimens from the same batch were machined into a size of 30 × 12 × 2 mm. These specimens were heat treated in an industrial vacuum furnace at a pressure of about $10^{-3}$mbar (0.1Pa): (1) the specimens were austenitized at 1293K for 2h followed by quenching by 5 bar (0.5MPa) nitrogen gas; (2) the specimens were then tempered twice at 843K for 2h and cooled in air. After the heat treatment, H13 substrate is fully

tempered martensite. A small hole (2mm in diameter) was drilled into each specimen and iron wires were threaded through to facilitate loading of specimens into the furnace. Then specimens were mechanically polished by the papers of different granulometry (320, 600, 1000 and 1500 mesh) to achieve a mirror finish. Finally, the specimens were ultrasonically cleaned in anhydrous ethanol and dried before liquid nitrocarburizing treatment.

Raw materials used for low-temperature liquid nitrocarburizing are non-toxic cyanate, chloride salt, and carbonate [31]. The nitrocarburizing process involved three steps: (1) melting the composite salt in the furnace; (2) immersing specimens in the molten salt at different temperatures (703/723/743K) and soaking for different time (4/8/12h); (3) air cooling. Concentration of $CNO^-$ in the molten salt bath in this experiment was above 40%. The nascent nitrogen utilized for nitrocarburizing reaction comes from the dissociation of $CNO^-$ by the following reactions: $4CNO^- \rightarrow CO_3^{2-} + 2CN^- + CO + 2[N]$ and CO: $2CO \rightarrow CO_2 + [C]$. Since the concentration of C is low, the latter reaction is limited by the low-temperature LNC treatment [32]. Active C and N atoms in the molten salt bath have such high chemical potentials that drive C and N diffuse into the AISI H13 die steel. Processing parameters of liquid nitrocarburizing are summarized in Table 1. To investigate the role and the importance of the oxide layer to the molten aluminum corrosion of nitrocarburized H13, the oxides on the surface of 743K 8h nitrocarburized specimen were removed for comparative study. Consequently, the effect of the nitrocarburized case on the molten aluminum resistance can be investigated separately. Mechanical polishing down to 0.5μm alumina powder was applied on polished specimens to remove the oxide layer after LNC treatments.

Table 1 Liquid nitrocarbuzing parameters

| Specimens codes | LNC temperature (K) | LNC time (h) | Polished or not |
|---|---|---|---|
| LNC 703 4/8/12 | 703 | 4/8/12 | no |
| LNC 723 4/8/12 | 723 | 4/8/12 | no |
| LNC 743 4/8/12 | 743 | 4/8/12 | no |
| LNC 743 8 polished | 743 | 8 | yes |

## 2.2 Characterization of the modified layers

The nitrocarburized cases were revealed by chemical etching with Nital (4% v/v nitric acid in analytically pure ethanol). Micrographs were acquired from cross sections of nitrocarburized cases using backscattered (BSE) and secondary electron (SE) signals in a SU-3500 scanning electron microscope (SEM). A SHIMADZU-1720 electron probe microanalyzer (EPMA) was used for

line-scan element compositional analysis. Hardness measurements were made by a HXD-1000TMC Digital Intelligent microhardness tester, with a test load of 100g and the holding duration of 15s for the nitrocarburized case and with a test load of 50g and the holding duration of 15s for the top hardness and the intermetallic compounds (IMC) layer hardness. The modified case thickness was measured to a depth where the hardness is 50 HV0.1 higher than that of the matrix, and the reported thickness value is an average of the 3 measurements and the error was calculated as the standard deviation of the 3 measurements. Cross sectional specimens were mounted in Bakelite and mirror-polished to 0.5μm alumina powder. The phase constituents were determined by EMPYREAN X-ray diffraction (XRD) using Cu-Kα radiation (λ=1.54Å). XRD patterns at different depths were obtained by grinding the samples after each XRD scan. Detailed experiment steps are as follows. Firstly, a XRD scan was carried out on the original treated sample surface with grinding. Then the thickness of the sample was measured by a spiral micrometer. Afterwards, the sample was grandly gently by P1500 SiC grinding paper (1500-mesh SiC paper with an average particle size of 12 μm). The sample thickness was measured again after the grinding using the spiral micrometer. Therefore, the depth of material removal can be estimated. Then the next XRD scan was carried out. This process was repeated until the measured XRD patterns is the same as the pattern of the H13 substrate.

## 2.3 Immersion test

H13 steel and nitrocarburized specimens were immersed in the molten alunminun which was melted in a graphite crucible (t=30min, T=1023K) and cooled in air to room temperature. The aluminum used in this experiment is 6063 aluminum alloy with the following chemical composition (wt %): 0.20-0.6 Si, 0.35 Fe, 0.10 Cu, 0.10 Mn, 0.45-0.9 Mg, 0.10 Cr, 0.10 Zn, 0.10Ti, and balance of aluminum. All immersion tests were repeated four times under the same condition. One of the specimens with residual aluminum was cut perpendicular to the solid/liquid interface for cross-sectional metallographic examinations using standard grinding and polishing procedure. Specimen microstructure was analyzed by SU-3500 scanning electron microscope (SEM) and line-scan element compositional examinations were carried out in the SHIMADZU-1720 electron probe microanalyzer (EPMA). The other three specimens were immersed in 10% saturated sodium hydroxide to remove residual aluminum and then cleaned in ethanol by ultrasounds for 5min. The weight loss during the immersion test was investigated based on gravimetric method, which is the change of the sample weight before and after the immersion test after the removal of the surface aluminum. Weight loss rate can be described by the weight change per square centimeter of the specimen per minute. Each weight loss rate value corresponded to an average of the 3 measurements and the error is calculated by standard deviation of the measurements.

# 3. Result and discussion

## 3.1 XRD analysis

To confirm the phase transformation of AISI H13 steel during the LNC treatments, XRD analysis was employed on the surface of the liquid nitrocarburized specimens. Figs. 1(a-c) showed that XRD patterns of LNC at 703K, 723K and 743K, respectively, and three different soaking time (4/8/12h) for each temperature. Phases were identified by matching patterns with powder crystallographic data, using the PDF cards #85-1410 (α'-Fe), 75-2140 ( $\alpha'_N$-Fe), 86-0231 ( $\gamma'$-$Fe_4N$), 83-0879 (ε-$Fe_3N$), and 72-2126 (ζ-$Fe_2N$).

XRD results of the liquid nitrocarburized AISI H13 specimens were depicted in Fig. 1(a). Matrix cubic martensite phase (α'-Fe) completely tranformed to tetragonal expended nitrogen-martensite phase ( $\alpha'_N$-Fe) [14] after liquid nitrocarburized at 703K and 4h, which proves the phase transformation sequence: α'-Fe + N/C → $\alpha'_N$-Fe. Extending the soaking time to 8h, the XRD result shows that modified layer is composed of $\alpha'_N$-Fe and $\gamma'$-$Fe_4N$. This explains that the gamma phase ( $\gamma'$-$Fe_4N$) did not transform from matrix α'-Fe phase or decomposed from ε-$Fe_3N$ but from $\alpha'_N$ -Fe phase, indicating the phase transformation sequence is $\alpha'_N$-Fe + N/C → γ'-$Fe_4N$. Furthermore, $\gamma'$-$Fe_4N$ phase would then quickly transform into close-packed hexagonal phase (ε-$Fe_3N$) in the outer surface area, where the N concentration can rapidly increase above 20 at%. The surface of the 723k 12h liquid nitrocarburized specimen is full of the mixture of ε-$Fe_3N$ and $\gamma'$-$Fe_4N$, manifesting the ε-$Fe_3N$ is precipitated from $\gamma'$-$Fe_4N$. Therefore, next step of reaction sequence is: γ'-$Fe_4N$ + N/C → ε-$Fe_3N$. Fig. 1(b) reveals modified layers are mainly composed of $\gamma$-$Fe_4N$ and ε-$Fe_3N$ phases at a relatively high temperature (723K). Whereas XRD patterns (Fig. 1(c)) of LNC 743K 8h and LNC 743K 12h show that the orthorhombic nitride phase (ζ-$Fe_2N$) dominates surface. The $\gamma'$-$Fe_4N$ and ε-$Fe_3N$ phase almost completely transformed into ζ-$Fe_2N$ phase during the soaking time 4-12h at 743K. The phase transformation during this process is: ε-$Fe_3N$ + N/C → ζ-$Fe_2N$. In addition, XRD results show that the iron oxide formed on the surface of LNC specimens at higher temperature and longer soaking time. The phase of oxide layer is duplex $Fe_3O_4$ and $Fe_2O_3$ at 743K 8h and 12h and $Fe_2O_3$ alone at 723K 8h and 12h as described in Figs. 1(b) and 1(c). The phase transformation mechanism can be summarized into:

α'-Fe + N/C→ $\alpha'_N$-Fe + N/C→ γ'-$Fe_4N$ + N/C→ ε-$Fe_3N$ + N/C→ ζ-$Fe_2N$.

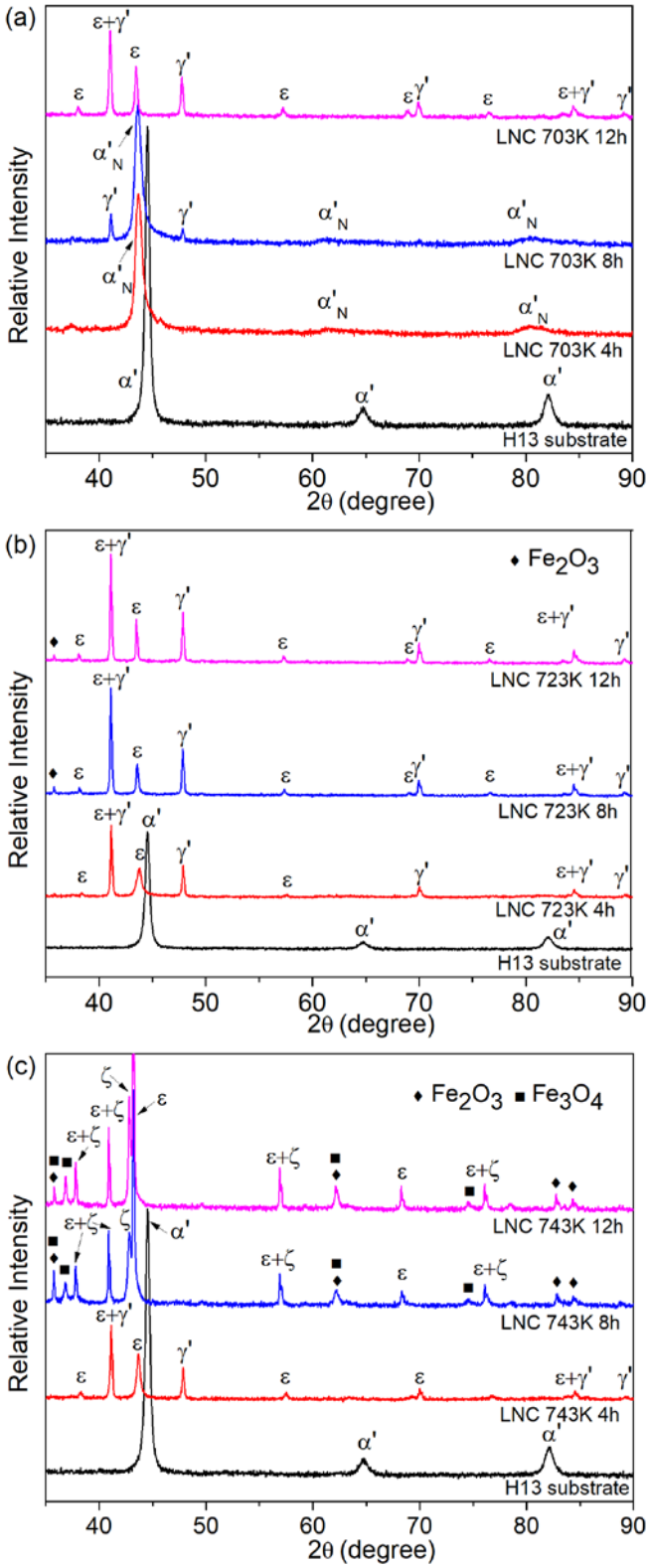


Fig. 1. XRD patterns of specimens: (a) H13 substrate and liquid nitrocarburized at 703K (b) H13 substrate and liquid nitrocarburized at 723K (c) H13 substrate and liquid nitrocarburized at 743K.

X-ray diffraction analysis for different depths of 743K 8h liquid nitrocarburized specimen is shown in Fig. 2 to study the phase distribution from surface to inner matrix. According to XRD

results, the outmost layer composed of duplex oxide $Fe_3O_4$ and $Fe_2O_3$ phases. At the depth of 6μm, the nitrocarburized layer is dominated by ε-$Fe_3N$ and ζ-$Fe_2N$ nitride phases. From 25μm to 63μm, nitride phases (ε-$Fe_3N$ and γ'-$Fe_4N$) prevail. Only $\alpha'_N$-Fe can be identified at the depth around 95μm and α'-Fe at the depth about 112μm is the matrix. The phases distribution of the nitrocarburized case is ε-$Fe_3N$ and ζ-$Fe_2N$ phase near the surface, ε-$Fe_3N$ and γ'-$Fe_4N$ phase in the transition layer, γ'-$Fe_4N$ and $\alpha'_N$-Fe near the matrix. This can be explained by the nature of diffusion, the nitrogen content reduces from surface to the inner matrix.

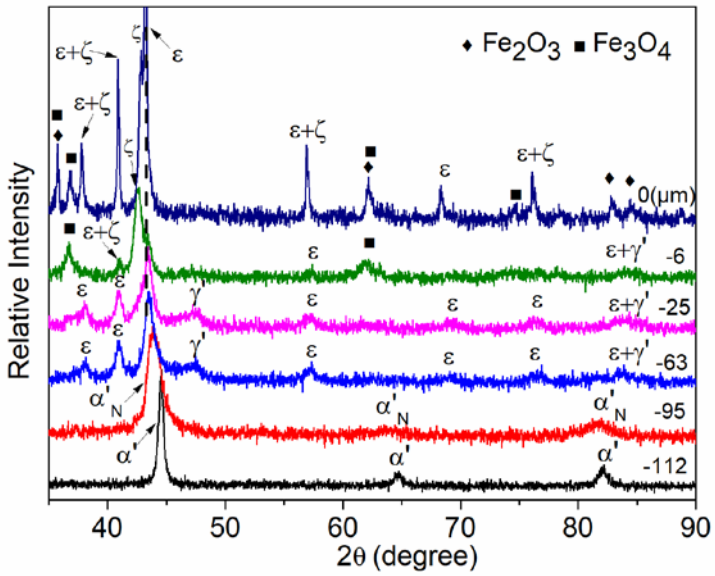


Fig. 2. XRD patterns of 743K 8h liquid nitrocarburized specimen for different depths.

## 3.2 Microstructure analysis

A typical micrograph of backscattered electronic image (BEI) from cross section of an AISI H13 die steel liquid nitrocarburized at 743K for 12h is shown in Fig. 3(a). It can be seen that the nitrocarburized specimen consists of four layers: an outermost oxide layer; a compound layer beneath the oxide layer; a diffusion layer below the compound layer and a transition layer between diffusion layer and matrix.

As shown in Fig. 3(b), the outmost oxide layer mainly consists of $Fe_2O_3$ and $Fe_3O_4$ with a thickness of about 4μm. The next is a well-studied homogeneous compound layer made up of iron nitride ε-$Fe_3N$ and ζ-$Fe_2N$ phase exhibited a thickness of approximately 10μm. It was also observed from cross-sectional secondary electronic images (SEIs) that the outmost part of the compound layers is uneven. It is known that the dark and serrated region is the oxides ($Fe_2O_3$ and $Fe_3O_4$) from the XRD result at the 6μm depth. The compound layer shows an uneven top surface due to the oxide formation during the process. Beneath the compound layer is a thick diffusion layer, in which the nitrogen atoms are incorporated into iron crystalline lattice, mainly composed

of ε-$Fe_3N$ and γ'-$Fe_4N$ phases. In some case, fine precipitation of nitrides of alloyed elements occurs simultaneously [33]. However, the volume fraction of these nitrides is so low that cannot be detected by XRD. Nitrogen diffusion coefficient along grain boundaries is much higher than that in the bulk, and thus nitride precipitates at grain boundaries during the process [34]. Especially, precipitation of CrN causes the formation of chromium-depleted regions near the grain boundaries, leading to preferentially-etching in diffusion layer [35]. Therefore, the diffusion layer presents dark and preferentially-etched in BEIs. Between diffusion layer and matrix, there is a transition layer etched slightly where the microhardness decreases progressively towards that of the matrix, principally containing α'-Fe phase with some γ'-$Fe_4N$ [36]. Fig. 3(d) shows distinct features of diffusion and transition layer on the morphology. The diffusion layer were etched severely and appeared to have more nitrides precipitations than the transition layer, which clearly revealed in Figs. 3(c) and 3(e). Nevertheless, the transition layer was more severely etched than matrix but less severely than the diffusion layer.

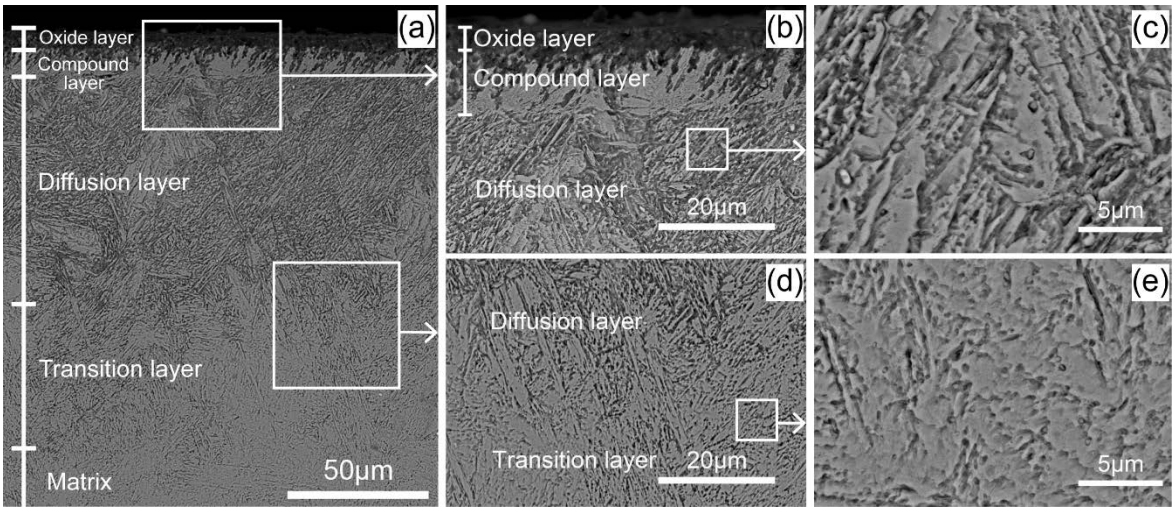


Fig. 3. (a) BEI cross-sectional micrograph of 743K 12h liquid nitrocarburized specimen. (b-e) BEI micrographs of different layers at various magnifications.

SEI cross-sectional micrographs of 703K/723K/743K 8h LNC specimens are shown in Figs. 4(a-c). Fig. 4(a) clearly shows that there is no oxide and compound layer forming at outmost surface of the specimen. The oxide layer and compound layer of the specimen LNC at 743K 8h (Fig. 4 (c)) are thicker than that of the specimen LNC at 723K 8h (Fig. 4(b)). The change of the oxide layer is consistent with previous XRD results (Fig. 1) and EPMA results (Fig. 4(e)). Figs. 4(d-f) reveal the elemental profile from the specimens of Figs. 4(a-c) obtained by EPMA close to the surface, indicating the nitrogen diffused deep into the matrix but the carbon and oxygen gathered on the surface. Nitrogen, oxygen and carbon mass content all increase as temperature increase. The phase content of the specimens can be deduced from the Fe-N diagram [37,

38]{Torchane, 1996 #13;Mittemeijer, 2013 #10}: the γ'-$Fe_4N$ phase forms when the nitrogen concentration is above 0.1 wt%; ε-$Fe_3N$ phase emerges when the nitrogen concentration is up to 5.9 wt% and the formation of ζ-$Fe_2N$ phase takes place when the nitrogen concentration is more than 11 wt%. The profile of nitrogen mass content (Fig. 4(d)) is consistent with the Fe-N diagram and the XRD results.

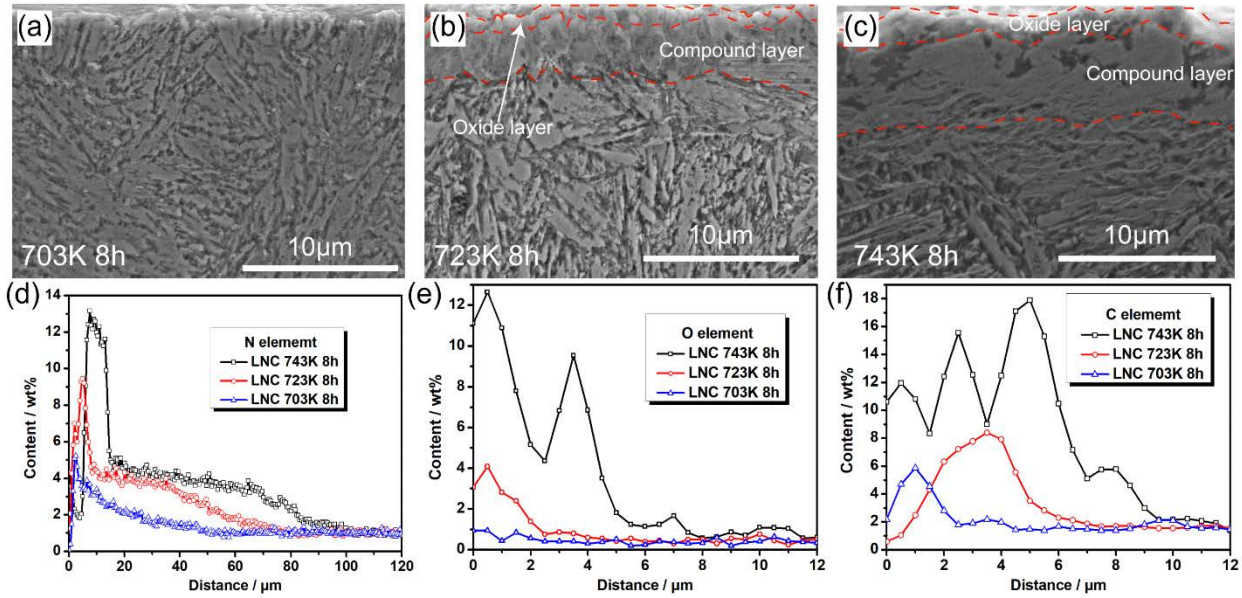


Fig. 4. (a-c) SEI cross-sectional micrographs of 703K/723K/743K 8h LNC specimens; (d-e) Nitrogen, carbon and oxygen element profiles of 703K/723K/743K 8h LNC specimens.

## 3.3 Microhardness and kinetics analysis

Fig. 5(a) shows the evolution of the cross sectional micro-hardness of specimens nitrocarburized under different process parameters. The profiles apparently indicate that the higher the treatment temperature is, the higher the hardening effect of liquid nitrocarburizing process does. This can be attributed to the diverse composition of the phase (Fig.1) in the modified layer. As expected, the hardness decreases with the increase of distance from surface, which is a distinguished diffusion feature, resulting from the expanded martensite (α'$_N$-Fe) formation and the presence of different nitrides phases in the LNC layer. Correlation of microhardness with microstructure (Figs. 3 and 4) is summarized in Fig. 5(c). Hardness of the compound layer is above 1100 $HV_{0.1}$, more than two times that of H13 substrate hardness (495.3 $HV_{0.1}$). The hardness of the diffusion layer decreased to 1000 $HV_{0.1}$ gradually, whereas the hardness of the transition layer decreased to the substrate hardness sharply. Hardness depth profile is attributed to the formation of iron nitrides (ε-$Fe_3N$ and ζ-$Fe_2N$) on the surface, which are much harder than γ′-$F_4N$ [39], and the C/N diffusion layer. As shown in Fig. 5(b), deepest nitrocarburized case (about 156μm) is produced after LNC at 743K 12h among different liquid nitrocarburing parameters. Case thickness

increases with longer LNC time, as well as higher temperature.

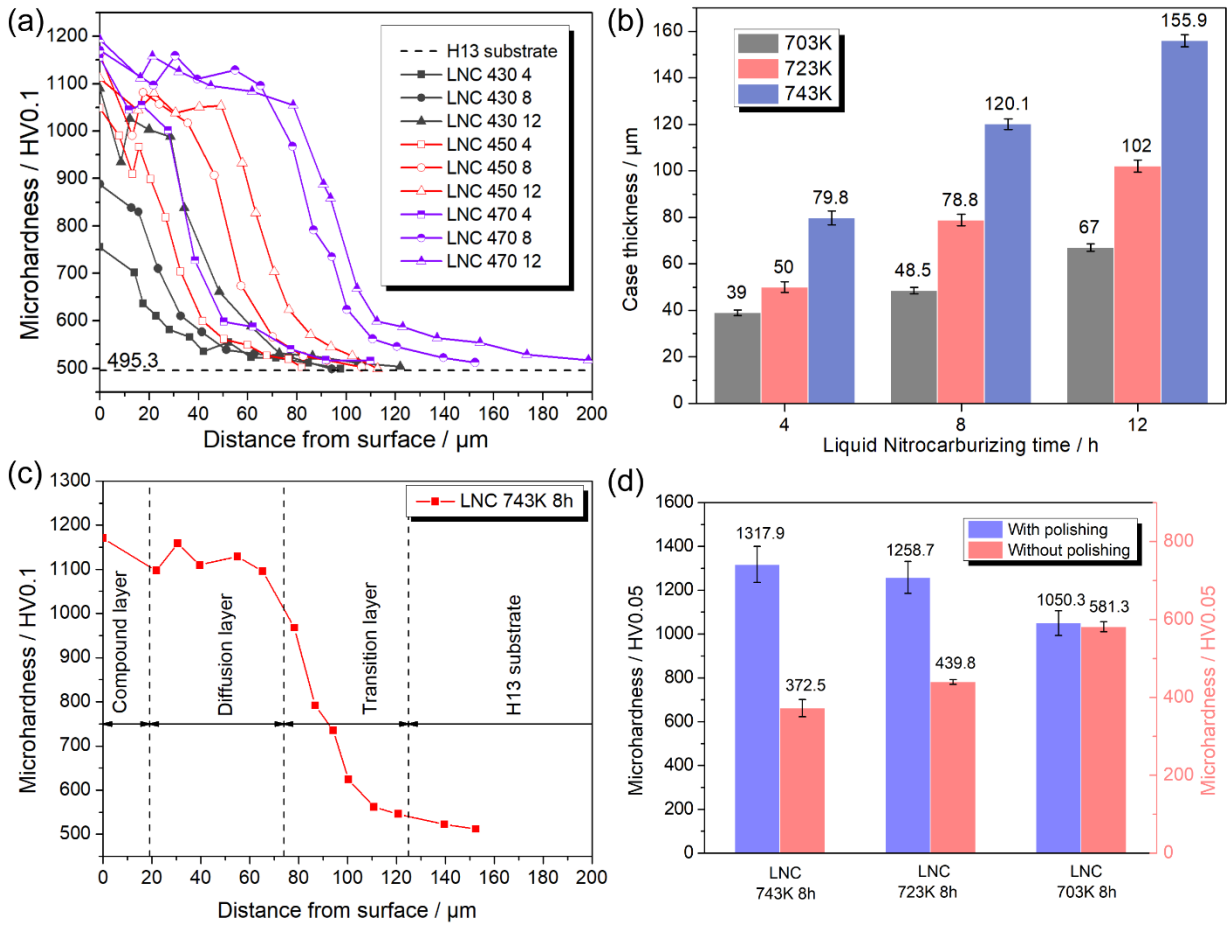


Fig. 5. (a) Cross-sectional microhardness profiles of liquid nitrocarburized specimens as a function of depth; (b) Nitrocarburized case thickness of different liquid nitrocarburizing parameters. (C) Correlations of microhardness with microstructure of LNC 743K 8h specimens. (d) Top surface hardness of LNC 703K/723K/743K 8h specimens with and without polishing.

In addition, the surface hardness with and without the presence of oxides is shown in Fig. 5(d). The top surface hardness decreased as the liquid nitrocarburizing temperature dropped from 743K to 703K in the absence of oxides. On the other hand, the top surface hardness increased as the liquid nitrocarbutizing temperature reduced without polishing (i.e. with oxides). This indicates that thickness of the oxides on sample surfaces increased as the temperature increased, given that the hardness of the oxides is much higher compared to nitrocarburized surface.

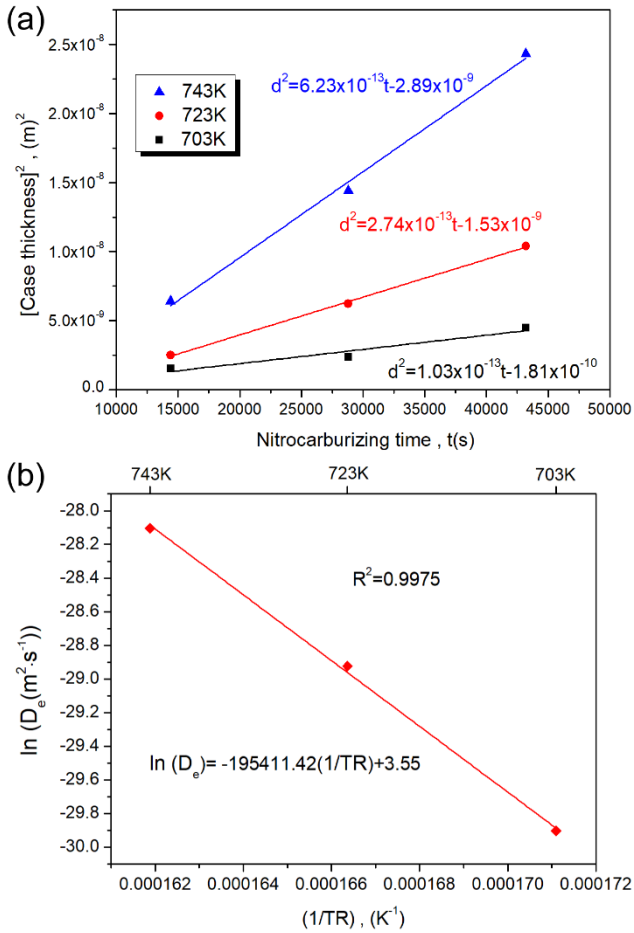


Fig. 6. (a) Nitrocarburized case thickness as a function of the square root of treatment time. (b) Arrhenius plot for the liquid nitrocarburized case thickness.

It is important to point out that temperature and time essentially control the diffusion rate and the concentration of the nitrogen on the surface layer, which decides the phase composition and results in the hardness of the liquid nitrocarburized specimens. In summary, the decisive factor of the hardness is the concentration of the nitrogen.

Assuming that progress of modified case obeys parabolic law, the squared thickness of modified case as a function of time can be described as follows [40] :

$$d^2 = D_e t + c \quad (1)$$

Where $d$ is case thickness, $D_e$ is diffusion coefficient depending on the treatment temperature, the constant $c$ is diffusion depth that is formed during heating time and $t$ is nitriding time. In order to obtain the nitrogen diffusion coefficient, the slope of the straight lines was considered in Fig. 6(a) adopted the data in Fig. 5(b).

The relationship between diffusion coefficient $D_e$ and temperature $T$, can be expressed by Arrhenius equation as follows [41] :

$$D_e = D_e^0 \exp(-\frac{Q}{RT}) \quad (2)$$

Taking the natural logarithm of both sides of Eq. (2),

$$\ln De = -\frac{Q}{RT} + \ln D_e^0 \quad (3)$$

Where $D_e^0$ is so-called pre-exponential factor, $Q$ is activation energy for diffusion, $R$=8.314 ($J \cdot mol^{-1}K^{-1}$) is the gas constant, and $T$ is absolute temperature.

The diffusion coefficient $D_e$ versus reciprocal treatment temperature is ploted in Fig. 6(b). The coefficient of correlation ($R^2$) of each correlation is 0.9975, and the activation energy is calculated as 195.4 $kJ \cdot mol^{-1}$. The data linearity for temperatures of 703K, 723K and 743K suggests that low-temperature liquid nitrocarburizing is a diffusion controlled process. The active energy Q can be used to predict the case thickness or to determine the treatment time and temperature for obtaining a predetermined case layer thickness [42].

## 3.4. Corrosion resistance to molten aluminum

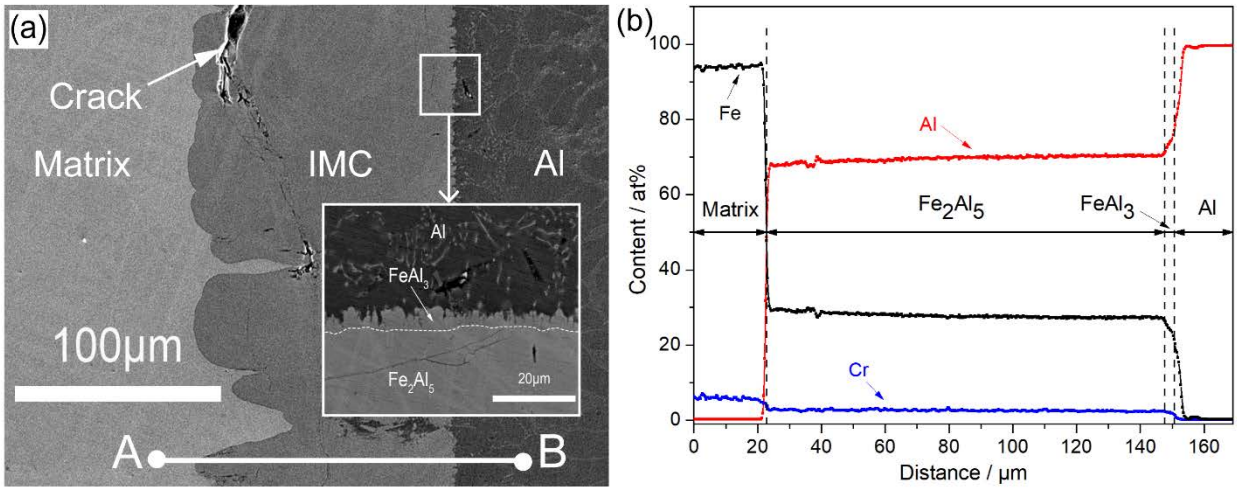


Fig.7 (a) Cross-sectional SEI micrograph of the interface of H13 substrate and 6063 aluminum (t =30min and T=1023K). (b) EPMA line-scan profiles of the interface of H13 substrate and 6063 aluminum (t =30min and T=1023K).

Fig. 7(a) shows the SE images of the H13 substrate immersed in 6063 aluminum at 1023K for 30min. In low magnification, it is clear that the tongue-like side of intermetallic compounds (IMC) layer is adjacent to H13 steel and the other flat side is adhere to aluminum. The cracks in the IMC layer were probably induced by the thermal stress between steel and aluminum or the formation of Kirkendall-porosity at the IMC layers [43, 44]. In high magnification, the IMC layer has formed from two composite layers: the serrated-like layer adjacent to the Al and the compact layer. Fig.

7(b) shows line-scan profiles from the AB straight line running across the H13 steel-aluminum interface. The distribution of iron, aluminum, and chromium is shown in this figure. The other elements of H13 are not detected due to low concentration. According to line-scan profile, iron and chromium concentration is reduced along AB line from point A to point B, but aluminum concentration is increased along AB line. Thus, the composite layer near the H13 contains more iron and the compact layer near the aluminum contains more aluminum. Al concentrations in the $Fe_2Al_5$ and $FeAl_3$ phase according to EPMA line-scan profiles (Fig. 7(b))are about 75 and 70 at.%, respectively, in good agreement with literature data [45].

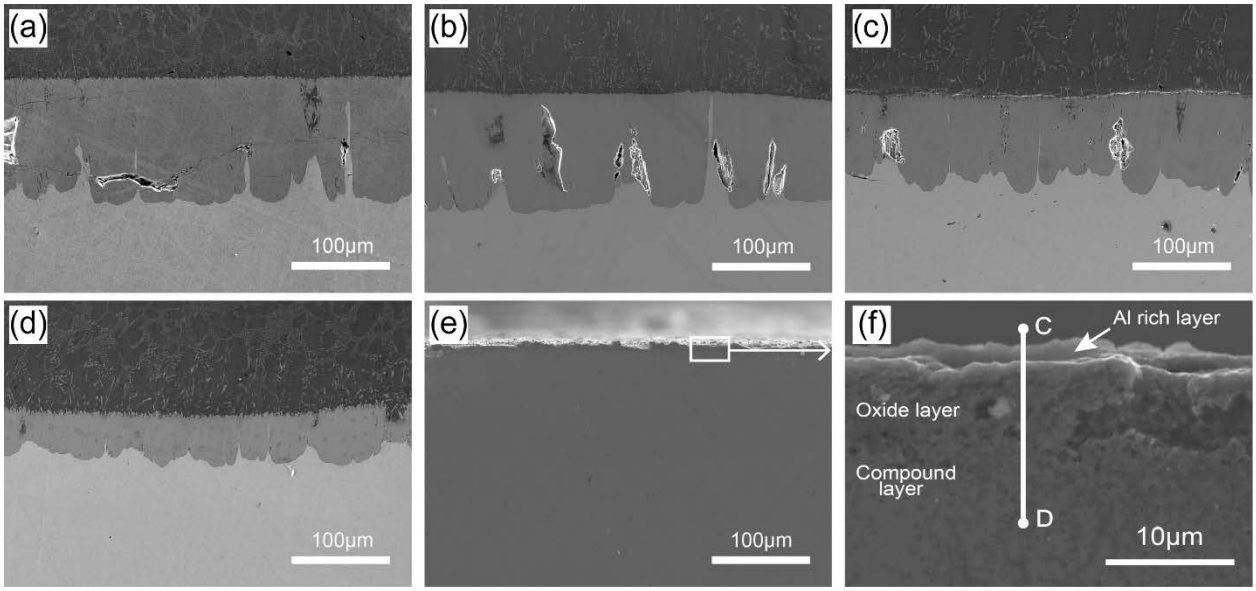


Fig. 8(a-e) Cross-sectional SEI micrographs of different processed H13 steel after immersion in molten aluminum (t =30min and T=1023K): (a) H13 substrate (b) 743K 8h polished (c) 703K 8h (d) 723K 8h (e) 743K 8h; (f) high magnification of (e).

Interfacial morphology of H13 specimens after different treatment immersed in molten aluminum are shown in Figs. 8(a-e). The treatment process of Fig. 8(a) to Fig. 8(e) is H13 substrate, 743K 8h polished, 703K 8h, 723K 8h and 743K 8h, respectively. The characterization of these interfaces is similar to Fig. 7(a) in low magnification, and IMC layers features the same phase composition but different thickness. In contrast, the specimen after 743K 8h liquid nitrocarburized did not form an intermetallic compounds layer as depicted in Fig. 8(e). In high magnification (Fig. 8(f)), there is a layer adheres to the oxide layer after immersion test. To confirm the element and phase composition of the layers, an EPMA line-scan of straight line CD and surface XRD analysis were employed. As shown in Fig. 9(a), the layer mainly contains aluminum element and little aluminum erosion into the oxide layer. Meanwhile, the oxide layer thickness almost doubled (about 8μm) during the immersion test, which indicated the oxide

element diffused into the compound layer. On the other hand, the XRD pattern of the surface shown in Fig. 9(b) also suggests the oxide layer of $Fe_2O_3$ and $Fe_3O_4$ transformed into phases of $Fe_3O_4$ and $Fe_{.9536}O$. The other phases identified on the surface are Al and $FeAl_2O_4$ which reveal this layer riches aluminum. It seems that molten aluminum is held back by this homogenous oxide layer.

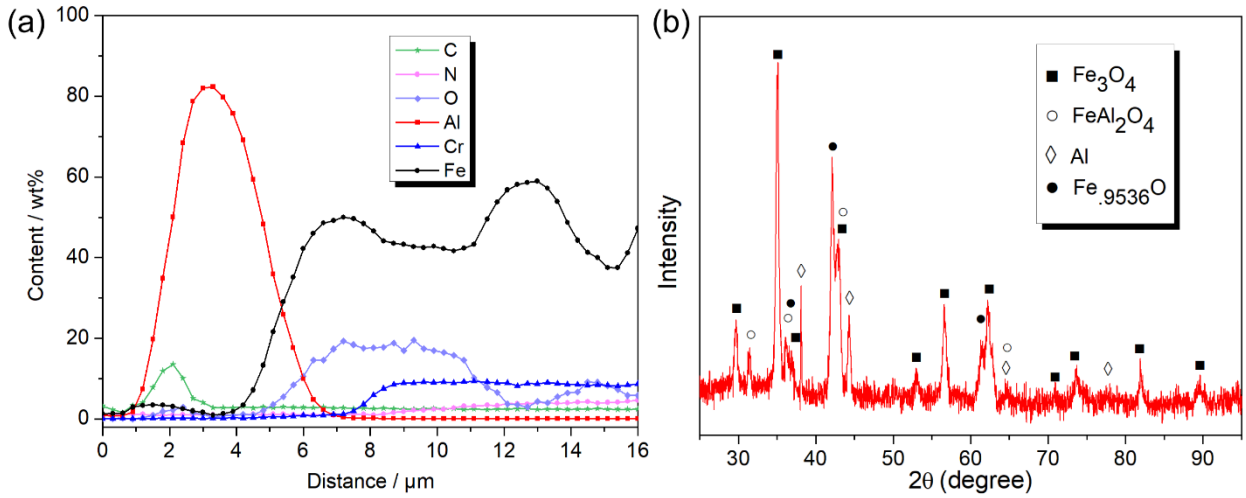


Fig. 9(a) EPMA line-scan profiles of straight CD in Fig. 8(f); (b) XRD pattern of 743K 8h nitrocarburized specimen after immersion test (t =30min and T=1023K).

In order to study the effect of the liquid nitrocarburized treatment on corrosion resistance in molten aluminum, the average thickness ($X_{mean}$) of the composite layer was evaluated by the following equation:

$$X_{mean} = \frac{A}{W} \tag{4}$$

Here, *A* and *W* are the total area and the total length of the composite layer, respectively, on the cross-section.

The average thickness ($X_{mean}$) and the weight loss rates ($mg \cdot cm^{-2} \cdot min^{-1}$) of the specimens immersed in molten aluminum are presented in Fig. 10. It should be noted that the average thickness (109.7μm) and the weight loss rate (1.904) of the 743K 8h and polished specimen are more than those of all other liquid nitrocarburized specimens. This demonstrates that a layer had formed during the liquid nitrocarburizing treatment as well as 703K 8h, and this layer is mainly composed of $Fe_2O_3$ and $Fe_3O_4$ oxide. Particularly, the average thickness (2.7μm) and the weight loss rate (0.072) of the 743K 8h treatment are very low, which exhibits an excellent corrosion resistance to molten Al. It must also be mentioned that the average thickness and the weight loss rate of the 743K 8h and polished specimen are a bit lower than these of H13 substrate, which indicated the nitriding layer to some extent exhibits corrosion resistance in molten aluminum due

to nitrocarburized case of the surface of H13 steel decreases the number and thickness of the intermetallic layers by delaying their growth kinetics [46].

According to the results of P.Tunthawiroon et al. [47], on specimens oxidized for shorter duration, $Fe_2O_3$ films were formed, which provided less effective corrosion resistance to molten Al than specimens oxidized for longer duration. In other words, the duplex film of $Fe_2O_3$ and $Fe_3O_4$ phase is more effective in improving corrosion resistance to molten Al than the $Fe_2O_3$ film, which is explicitly expressed by smaller $X_{mean}$ and the lower weight loss rates of liquid nitrocarburized 743K 8h specimens than those of the liquid nitrocarburized 723K 8h.

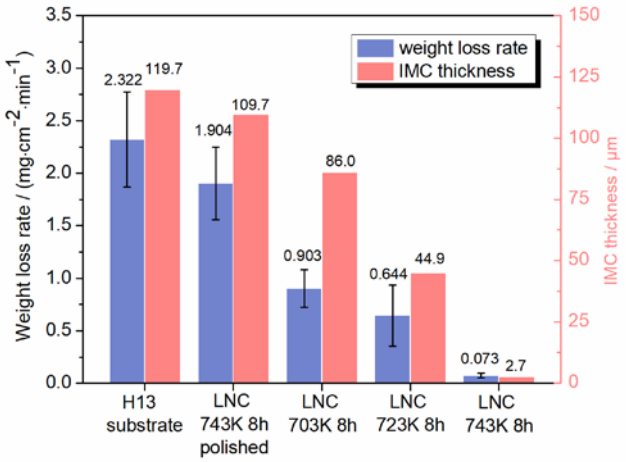


Fig.10 Weight loss of per square decimeter per minute of the specimens immersed in molten aluminum (t =30min and T=1023K) and the IMC thickness of these specimens.

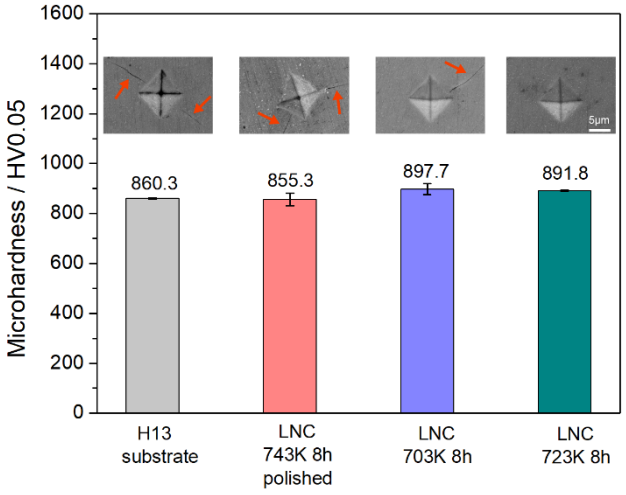


Fig. 11 Hardness and indentations of the intermetallic compounds (IMC) layers formed by the immersion test.

As shown in Fig. 8, thickness of IMC layers depends on the nitrocarburizing parameters. It is also observed that there are more cracks in IMC layer on specimen treated at 743K 8h than those on specimens treated at 703k 8h and 723K 8h. Therefore, indentation was carried out on these

IMC layers, in order to identify the hardness of LNC treated surfaces without polishing and the results are shown in Fig 11. Hardness of IMC layer on H13 substrates and polished 743K 8h specimens is slightly lower than that of 703k 8h and 723K 8h liquid nitrocarburized specimens. Lower hardness can be attributed to the crack formation (pointed by red arrows in Fig. 11). Two cracks appear on the corners of the indentations on H13 substrate and 743K 8h polished specimen. This suggests that the IMC layers are low in fracture toughness and thus cracks can easily form during indentation. On the contrast, there is only one crack around the indentation on the sample nitrocarburized at 703K for 8h. No crack was observed around the indentation of the IMC layers on LNC treated at 723K 8h. This suggests that liquid nitrocarburizing treatment enhances the fracture toughness of IMC layers and thus reduce its tendency to cracks. It is clear by correlating weight loss (Fig. 10) with the cracking tendency (Fig.11) that the higher the tendency to crack, the greater the weight loss.

To investigate the effect of liquid nitrocarburing treatment on corrosion resistance to molten aluminum, schematic illustrations of H13 substrate and liquid nitrocarburized specimen in molten aluminum are depicted in Fig. 12(a-c), and (d-f), respectively.

The whole process of corrosion can be divided into two parts: diffusion and reaction. The interfacial reactions are considered to start with the mutual diffusion of Al and H13, meanwhile the Al reacted with H13 resulting of the formation of the intermetallic phases (Fig. 12(b)). After 30min diffusion and reaction, an IMC layer formed at the interface (Fig. 12(c)). The IMC layers are made up of thin $FeAl_3$ phase layer and $Fe_2Al_5$ phase layer due to the $Fe_2Al_5$ phase is the major constituent of the reaction layer [48].

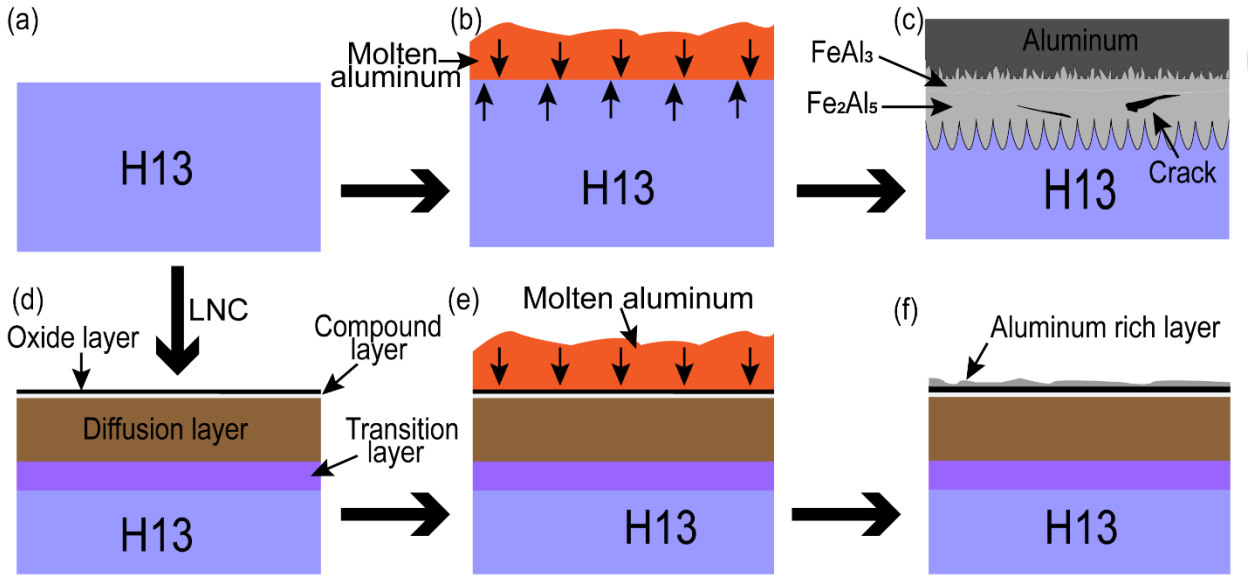


Fig. 12. Schematic illustration of corrosion resistance to molten aluminum enhanced by 743K 8h liquid nitrocarburing treatment.

The microstructure of the specimens after LNC treatment generally formed about four layers near the surface. From the surface to the matrix are oxide layer, compound layer, diffusion layer and transition layer, respectively. Furthermore, compound layer, diffusion layer and transition layer are generally known as nitrocarburized layer which presents low effect on corrosion resistance in molten aluminum immersion test. Oxide layer formed during the LNC process provides better corrosion resistance to molten aluminum. Nevertheless, the phase composition and the thickness of the oxide layer determine the corrosion resistance to molten aluminum. $Fe_2O_3$ phase reacts with molten aluminum so it provides less improvement on corrosion resistance. A complex oxide layer of $Fe_2O_3$ and $Fe_3O_4$, formed at 743K, provides an excellent effect on corrosion resistance to molten aluminum. The oxide layer is a diffusion barrier in molten aluminum, thus there will be very limited matrix to diffusion into molten aluminum. On the other hand, though the molten aluminum still has a trend to diffuse into oxide layer, it cannot penetrate the oxide layer during the immersion period, only to formed an aluminum rich layer on the oxide layer (Fig. 12(f)). Therefore, the corrosion resistance to molten aluminum greatly enhanced by the oxide layer due to prevention of the interdiffusion between H13 and molten aluminum. The corrosion resistance to molten aluminum of the oxide layer may be related to wetting properties of the molten aluminum on oxide surface.

## 4. Conclusions

The effect of liquid nitrocarburizing treatment on the corrosion resistance of H13 steel to molten aluminum has been investigated. Based on the detailed microstructual characterization and the kinetics studies, a mechanism has been discussed, which involved in the improved corrosion resistance of liquid nitrocarburized H13 steel to molten aluminum. Based on results the following conclusions can be drawn:

(1) The phase composition and the hardness of the specimens can be controlled by the parameter of low-temperature liquid nitrocarburizing treatment.

(2) The phase transformations mechanism or sequence for liquid nitrocarburing treatment of H13 steel can be described as: $\alpha' + N/C \rightarrow \alpha'_N + N/C \rightarrow \gamma' + N/C \rightarrow \varepsilon + N/C \rightarrow \zeta$.

(3) Liquid nitrocarburizing treatment has greatly improved the hardness of the modified layer. The hardness value of the compound layer was above $1100HV_{0.1}$, and the thick diffusion layer features a hardness of above 1000 $HV_{0.1}$. The kinetics of layer growth depends on processing temperature and time. It can also be concluded that low-temperature nitrocarburizing is a diffusion controlled process. The calculated activation energy for nitrocarburizing layer growth is 195.4 kJ $mol^{-1}$.

(4) The corrosion resistance to molten aluminum can be improved by the low-temperature liquid nitrocarburing treatment. Although the nitrocarburized layers have low effect on corrosion resistance, the oxide layer formed during the low-temperature liquid nitrocarburizing treatment performed better corrosion resistance. A duplex oxide layer of $Fe_2O_3$ and $Fe_3O_4$ is more effective on improving corrosion resistance to molten aluminum than the single $Fe_2O_3$ phase oxide layer.

## Acknowledgements

Authors are very grateful to the grant of National Natural Science Foundation of China (No. 51471112, 51611130204, and 51801194), the Science and Technology Planning Project of Sichuan (No.2016GZ0173), the Sichuan applied basic research project (2018JY0430), and the Newton Mobility Grant from Royal Society, UK (IE151027) for the financial support of this research. The author (J.W) would like to thank Dr.Jianru Fang at Foundry Mould Committee of China for their valuable discussion during the course of the research and writing.

## Reference

[1] R.L.O. Basso, H.O. Pastore, V. Schmidt, I.J.R. Baumvol, S.A.C. Abarca, F.S. de Souza, A. Spinelli, C.A. Figueroa, C. Giacomelli, Microstructure and corrosion behaviour of pulsed plasma-nitrided AISI H13 tool steel, Corrosion Science, 52 (2010) 3133-3139.

[2] G. Castro, A. Fernández-Vicente, J. Cid, Influence of the nitriding time in the wear behaviour of an AISI H13 steel during a crankshaft forging process, Wear, 263 (2007) 1375-1385.

[3] M. Tercelj, A. Smolej, P. Fajfar, R. Turk, Laboratory assessment of wear on nitrided surfaces of dies for hot extrusion of aluminium, Tribology International, 40 (2007) 374-384.

[4] M. Zhou, K. Li, D. Shu, B.D. Sun, J. Wang, Corrosion resistance properties of enamels with high B203–P205 content to molten aluminum, Materials Science and Engineering: A, 346 (2003) 116-121.

[5] W. Deqing, S. Ziyuan, Z. Longjiang, A liquid aluminum corrosion resistance surface on steel substrate, Applied Surface Science, 214 (2003) 304-311.

[6] Q. Wang, W.J. Wang, H.J. Liu, C.L. Zeng, Corrosion behavior of zirconium diboride coated stainless steel in molten 6061 aluminum alloy, Surface and Coatings Technology, 313 (2017) 129-135.

[7] A.F.M. Arif, A.K. Sheikh, S.Z. Qamar, A study of die failure mechanisms in aluminum extrusion, Journal of Materials Processing Technology, 134 (2003) 318-328.
[8] X. Zhang, X. Li, W. Chen, Interfacial reactions of duplex stainless steels with molten aluminum, Surface and Interface Analysis, 47 (2015) 648-656.
[9] X.-m. Zhang, W.-p. Chen, Review on corrosion-wear resistance performance of materials in molten aluminum and its alloys, Transactions of Nonferrous Metals Society of China, 25 (2015) 1715-1731.
[10] E.J. Mittemeijer, J.T. Slycke, CHEMICAL POTENTIALS AND ACTIVITIES OF NITROGEN AND CARBON IMPOSED BY GASEOUS NITRIDING AND CARBURISING ATMOSPHERES, Surface Engineering, 12 (1996) 152-162.
[11] T. Bell, Y. Sun, A. Suhadi, Environmental and technical aspects of plasma nitrocarburising, Vacuum, 59 (2000) 14-23.
[12] H.S. Cho, T. Bell, Effect of cooling rate on plasma nitrocarburised compound layers for pure iron, Metals and Materials International, 8 (2002) 93-98.
[13] W.L. Chen, C.L. Wu, Z.R. Liu, S. Ni, Y. Hong, Y. Zhang, J.H. Chen, Phase transformations in the nitrocarburizing surface of carbon steels revisited by microstructure and property characterizations, Acta Materialia, 61 (2013) 3963-3972.
[14] V. Leskovsek, M. Godec, P. Kogej, Influence of low-temperature nitriding on the strain-induced martensite and laser-quenched austenite in a magnetic encoder made from 304L stainless steel, Sci Rep, 6 (2016) 30979.
[15] K. Nakasa, A. Yamamoto, R. Wang, T. Sumomogi, Effect of plasma nitriding on the strength of fine protrusions formed by sputter etching of AISI type 420 stainless steel, Surface and Coatings Technology, 272 (2015) 298-308.
[16] F. Borgioli, E. Galvanetto, T. Bacci, Influence of surface morphology and roughness on water wetting properties of low temperature nitrided austenitic stainless steels, Materials Characterization, 95 (2014) 278-284.
[17] S.D. Jacobsen, R. Hinrichs, I.J.R. Baumvol, G. Castellano, M.A.Z. Vasconcellos, Depth distribution of martensite in plasma nitrided AISI H13 steel and its correlation to hardness, Surface and Coatings Technology, 270 (2015) 266-271.
[18] Y.X. Wang, Z.B. Chen, M.F. Yan, C.S. Zhang, H.T. Chen, Y.D. Zhu, Preparation and characterization of ultra-refined expanded martensite α’N, Surface and Coatings Technology, 326 (2017) 216-223.

[19] B. Wang, X. Zhao, W. Li, M. Qin, J. Gu, Effect of nitrided-layer microstructure control on wear behavior of AISI H13 hot work die steel, Applied Surface Science, 431 (2018) 39-43.
[20] J. Chen, X.Y. Li, T. Bell, H. Dong, Improving the wear properties of Stellite 21 alloy by plasma surface alloying with carbon and nitrogen, Wear, 264 (2008) 157-165.
[21] M.L. Doche, V. Meynie, H. Mazille, C. Deramaix, P. Jacquot, Improvement of the corrosion resistance of low-pressure nitrided and post-oxidized steels by a polymer impregnation final treatment, Surf. Coat. Technol., 154 (2002) 113-123.
[22] N. Karimzadeh, E.G. Moghaddam, M. Mirjani, K. Raeissi, The effect of gas mixture of post-oxidation on structure and corrosion behavior of plasma nitrided AISI 316 stainless steel, Applied Surface Science, 283 (2013) 584-589.
[23] H.R. Abedi, M. Salehi, M. Yazdkhasti, A. Hemmasian-E, Effect of high temperature post-oxidizing on tribological and corrosion behavior of plasma nitrided AISI 316 austenitic stainless steel, Vacuum, 85 (2010) 443-447.
[24] S.-H. Chang, T.-P. Tang, K.-T. Huang, J.-K. Chen, Effects of Post-oxidizing Treatment on Melting Loss and Corrosion Resistance of Gas Nitrided AISI H13 Tool Steel, Isij International, 52 (2012) 499-504.
[25] S.-H. Chang, T.-P. Tang, K.-T. Huang, Improvement of Aluminum Erosion Behavior and Corrosion Resistance of AISI H13 Tool Steel by Oxidation Treatment, Isij International, 50 (2010) 569-573.
[26] S.-H. Chang, T.-P. Tang, Y.-C. Chen, J.-K. Chen, Enhancement of Erosion Resistance on AISI H13 Tool Steel by Oxynitriding Treatment, Isij International, 49 (2009) 421-424.
[27] K. Funatani, Low-temperature salt bath nitriding of steels, Metal Science and Heat Treatment, 46 (2004) 277-281.
[28] Y.H. Qiang, S.R. Ge, Q.J. Xue, Study on the structure and wear resistance of two-step salt bath nitrocarburized steel, Wear, 218 (1998) 232-236.
[29] F. Bottoli, M.S. Jellesen, T.L. Christiansen, G. Winther, M.A.J. Somers, High temperature solution-nitriding and low-temperature nitriding of AISI 316: Effect on pitting potential and crevice corrosion performance, Applied Surface Science, 431 (2018) 24-31.
[30] C. Nan, D.O. Northwood, R.J. Bowers, X. Sun, P. Bauerle, The use of navy C-ring specimens to study distortion in ferritic nitrocarburized 1010 steel, 1 (2009) 13-25.

[31] X. Zhang, J. Wang, H. Fan, D. Pan, Erosion–corrosion resistance properties of 316L austenitic stainless steels after low-temperature liquid nitriding, Applied Surface Science, 440 (2018) 755-762.
[32] J. Wang, Y. Lin, Q. Zhang, D. Zeng, H. Fan, Effect of Treatment Time on the Microstructure of Austenitic Stainless Steel During Low-Temperature Liquid Nitrocarburizing, Metallurgical and Materials Transactions A, 45 (2014) 4525-4534.
[33] F. Lantelme, H. Groult, H. Mosqueda, P.-L. Magdinier, H. Chavanne, V. Monteux, P. Maurin-Perrier, Salt Bath Thermal Treating and Nitriding, (2013) 101-129.
[34] W. Chen, C. Wu, J. Chen, A. He, An Electron Microscopy Study of Vein-like Grain Boundary Microstructure in Nitrocarburized Low Carbon Steels, Journal of Materials Science & Technology, 29 (2013) 669-672.
[35] J.W. Simmons, D.G. Atteridtge, J.C. Rawers, SENSITIZATION OF HIGH-NITROGEN AUSTENITIC STAINLESS-STEELS BY DICHROMIUM NITRIDE PRECIPITATION, Corrosion, 50 (1994) 491-501.
[36] P. Psyllaki, G. Kefalonikas, G. Pantazopoulos, S. Antoniou, J. Sideris, Microstructure and tribological behaviour of liquid nitrocarburised tool steels, Surface and Coatings Technology, 162 (2003) 67-78.
[37] H. Jacobs, D. Rechenbach, U. Zachwieja, STRUCTURE DETERMINATION OF GAMMA'-FE4N AND EPSILON-FE3N, Journal of Alloys and Compounds, 227 (1995) 10-17.
[38] H.A. Wriedt, N.A. Gokcen, R.H. Nafziger, The Fe-N (Iron-Nitrogen) system, Bulletin of Alloy Phase Diagrams, 8 (1987) 355-377.
[39] J.-S. Chen, C. Yu, H. Lu, Phase stability, magnetism, elastic properties and hardness of binary iron nitrides from first principles, Journal of Alloys and Compounds, 625 (2015) 224-230.
[40] K. Genel, Boriding kinetics of H13 steel, Vacuum, 80 (2006) 451-457.
[41] S.X. Liang, L.X. Yin, X.Y. Liu, X.X. Wu, M.Z. Ma, R.P. Liu, Kinetics of thermodiffusion of TZ20 titanium alloy gas-nitride within temperature of 500 °C–650 °C, Journal of Alloys and Compounds, 734 (2018) 172-178.
[42] Z. Zhou, M. Dai, Z. Shen, J. Hu, Effect of D.C. electric field on salt bath nitriding for 35 steel and kinetics analysis, Journal of Alloys and Compounds, 623 (2015) 261-265.
[43] J. Rong, Z. Kang, S. Chen, D. Yang, J. Huang, J. Yang, Growth kinetics and thickness prediction of interfacial intermetallic compounds between solid steel

and molten aluminum based on thermophysical simulation in a few seconds, Materials Characterization, 132 (2017) 413-421.
[44] H. Springer, A. Kostka, J.F. dos Santos, D. Raabe, Influence of intermetallic phases and Kirkendall-porosity on the mechanical properties of joints between steel and aluminium alloys, Materials Science and Engineering: A, 528 (2011) 4630-4642.
[45] H.J. Springer, A. Kostka, E. Payton, Funtamental research into the role of intermetallic phases in joining of alluminum alloys to steel, 2010.
[46] K.A. Nazari, S.G. Shabestari, Effect of micro alloying elements on the interfacial reactions between molten aluminum alloy and tool steel, Journal of Alloys and Compounds, 478 (2009) 523-530.
[47] P. Tunthawiroon, Y. Li, N. Tang, A. Chiba, Enhancement of corrosion resistance of Fe–Cr–Mo alloy to molten Al by thermal oxidation in air, Corrosion Science, 77 (2013) 97-102.
[48] H. Springer, A. Kostka, E.J. Payton, D. Raabe, A. Kaysser-Pyzalla, G. Eggeler, On the formation and growth of intermetallic phases during interdiffusion between low-carbon steel and aluminum alloys, Acta Materialia, 59 (2011) 1586-1600.